energies

MDPI

Article

A New Method for State of Charge Estimation of Lithium-Ion Batteries Using Square Root Cubature Kalman Filter

Xiangyu Cui [1], Zhu Jing [1,2,*], Maji Luo [3], Yazhou Guo [3] and Huimin Qiao [1]

1 State Key Laboratory of Advanced Design and Manufacture for Vehicle Body, Hunan University, Changsha 410082, China; cuixiangyu@hnu.edu.cn (X.C.); kingniao@gmail.com (H.Q.)
2 Haima Automobile Group Co., Ltd., Haikou 570216, China
3 Hubei Key Laboratory of Advanced Technology for Automotive Components, Wuhan University of Technology, Wuhan 430070, China; mysm1203@163.com (M.L.); kingniao2000@163.com (Y.G.)
* Correspondence: jingzhu01@hnu.edu.cn; Tel.: +86-731-8882-2640

Received: 22 December 2017; Accepted: 8 January 2018; Published: 15 January 2018

Abstract: State of charge (SOC) is a key parameter for lithium-ion battery management systems. The square root cubature Kalman filter (SRCKF) algorithm has been developed to estimate the SOC of batteries. SRCKF calculates $2n$ points that have the same weights according to cubature transform to approximate the mean of state variables. After these points are propagated by nonlinear functions, the mean and the variance of the capture can achieve third-order precision of the real values of the nonlinear functions. SRCKF directly propagates and updates the square root of the state covariance matrix in the form of Cholesky decomposition, guarantees the nonnegative quality of the covariance matrix, and avoids the divergence of the filter. Simulink models and the test bench of extended Kalman filter (EKF), Unscented Kalman filter (UKF), cubature Kalman filter (CKF) and SRCKF are built. Three experiments have been carried out to evaluate the performances of the proposed methods. The results of the comparison of accuracy, robustness, and convergence rate with EKF, UKF, CKF and SRCKF are presented. Compared with the traditional EKF, UKF and CKF algorithms, the SRCKF algorithm is found to yield better SOC estimation accuracy, higher robustness and better convergence rate.

Keywords: lithium-ion batteries; state of charge (SOC); square root cubature Kalman filter (SRCKF); electric vehicle (EV); real-time estimation

1. Introduction

Increasingly along with the fossil energy depletion, air pollution and more and more serious global climate changes, people have begun to realize the great importance of the utilization and development of non-fossil energy [1]. Governments all over the world have introduced a variety of incentives to reduce pollutant emissions and greenhouse gas emissions [2–6]. Since transportation consumes a large amount of energy, it is necessary to develop and utilize electric vehicles (EVs) to realize green mobility. Lithium-ion batteries (LIBs) have many advantages, such as high power density and durability, and therefore they have been widely used in EVs. However, when overcharging occurs, the LIBs are more likely to burn and explode than other batteries, necessitating higher requirements for battery management system (BMS) [7–10]. A few parameters, such as maximum discharge current, specific energy of weight, specific energy of volume, and power density, determine an EV's performance [11–15]. The most important index for a BMS is state of charge (SOC). Because of the inherently time-varying and non-linearity characteristics of LIB under working conditions, accurate estimation of SOC remains a challenge [16–19].

1.1. Review of Methods

Some popular methods for SOC estimation are discussed below.

The open-circuit voltage method is simple and easy to use. SOC estimation in the late and early stages of charging is effective, but batteries must be tested online for a long time. This approach is used to estimate the charging efficiency of battery packs in laboratories and the accuracy of SOC estimation [10,19–21].

The neural network model method can realize basic nonlinear characteristics and can give corresponding outputs to external excitation. This method can also be used to simulate the characteristics of the nonlinear dynamic of batteries. The main problem with this method is that a large amount of reference data are required to be trained, and the estimation error of SOC is significantly impacted by the approach and data. Other flaws are that this method consumes considerable computer time in BMS applications, high demands for the BMS design, and high costs to adopt high-performance chips, which obviously cannot meet the requirements in the competitive automobile industry; consequently, the method cannot be used in mass production of electric vehicles [22].

Particle filter (PF) [23] and unscented PF [24,25] perform efficiently in nonlinear and non-Gaussian estimation. However, the major issue is that a complex BMS environment requires considerable sample data to describe posterior probability distribution. Other flaws are similar to those of neural network approaches [26–30].

The extended Kalman filter (EKF) is a typical representative of traditional nonlinear estimation approaches. The basic idea is to locally linearize a nonlinear state and the functions of measurement to perform a first-order Taylor polynomial expansion and then apply the Kalman filter formula of linear systems. EKF requires that the state and measurement functions of nonlinear systems be continuously differentiable, which limits its application scope. The first-order linearization approximation of nonlinear functions leads to low estimation accuracy, especially when systems are strongly nonlinear and the EKF estimation precision is severely reduced or even divergent. The Jacobin matrix of nonlinear functions should be calculated, which can easily cause differential stability of EKF and calculation divergence [31–36].

Unscented Kalman filter (UKF) [37] differs from EKF in that it replaces the first-order Taylor expansion in EKF with unscented transform (UT). UKF selects $2n + 1$ sigma points with weight according to UT to approximate the mean of state variables. After the sigma points are propagated by nonlinear functions, the mean and the variance of the capture can achieve third-order precision of the real values of the nonlinear functions; thus, the precision of UKF is higher than that of EKF [38]. Nevertheless, UKF needs to compute and transform the sigma points, which leads to a high computational complexity and cost of BMS.

In cubature Kalman filter (CKF), the mean and the variance of the system state are propagated through $2n$ equal-weight cubature points, which enables it to obtain high estimation accuracy. CKF, on the basis of cubature criteria, gives new points after the transformation of nonlinear system equations from $2n$ cubature points that have equal weight values to give the estimation of the system state at the next time. The cubature point and its weight are only determined by the state dimension and can be calculated and stored in advance. CKF can reduce computation time while maintaining estimation accuracy because of its use of minimal sampling points, and it is gradually replacing UKF as the filtering method for embedded system applications [39]. The CKF algorithm in engineering applications is susceptible to abnormal perturbation, inexact initial values, and difficulty in decomposing non-semi-definite matrices with Cholesky, which leads to system divergence [40].

In addition to the above methods, data-driven approaches, such as sliding mode observer [41], H-infinity observer [42], recursive further squares [43], EKF-based methods with online parameter identification [44,45], the Lyapunov-based estimator [46], and an estimation of the SOC and the model parameters simultaneously with paralleled filters [47–50] have also been studied. Most of these methods require adequate incentives. If the incentives are not obvious (such as charging condition), these methods are not very good for SOC estimation. These methods can solve some particular

problems with certain requirements, but these methods cannot be good for the robustness [13,51] and anti-measurement noise interference. In addition, there are other methods based on electrochemical models [52,53] that have been reported. However, because of the complexity (strict electrode dynamic theoretical framework and a large number of battery data accumulation) of these methods, they are not suitable for real BMS.

In real conditions, most controllers use embedded micro-controller units to compute the algorithm and control logic. Under the finite computing resources of embedded micro-controller units, the method for SOC estimation must not be complex and must have a rapid convergence speed and anti-measurement of noise interference to increase the robustness of BMS. Through what has been reviewed above, some requirements have not been fully met. We proposed a new method for SOC estimation using the square root cubature Kalman filter (SRCKF) algorithm in this paper. The SRCKF is based on CKF, directly propagates and updates the square root of the state covariance matrix in the form of Cholesky decomposition, obtains higher computational efficiency, guarantees the non-negative qualitative of the covariance matrix, avoids the divergence of the algorithm, and improves the convergence speed and stability of the filter.

1.2. Contribution of This Study

This paper aims to develop a new method based on the Thevenin model. The new method can improve the accuracy, robustness, and convergence rate of SOC estimation. The SRCKF algorithm is different from EKF and UKF algorithms, uses the cubature principle for nonlinear state particles and presents robustness in extreme nonlinear conditions. Compared with the EKF method, the present method can enhance SOC estimation accuracy and robustness and improve the convergence rate. When compared with the UKF method, the computation cost can be reduced with better estimation accuracy of SOC and robustness. Compared with the CKF approach, the present method can enhance the robustness and convergence rate with the same SOC estimation. Furthermore, the SRCKF algorithm has a better capability to overcome disturbances of unstable noises for SOC estimation. Thus, it can ensure the robustness and estimation accuracy of the algorithm in the case of limited computing resource requirements and can be applied to new BMS with online SOC estimation easily.

1.3. Organization of This Paper

The remaining sections of this paper are structured as follows. Section 2 discusses the parameters of the dynamic LIB model. Section 3 elucidates the principles of the SRCKF algorithm of SOC estimation. Section 4 shows the experimental configurations and the results of the parameters of the lithium-ion battery model identified offline. Experimental results and discussion are presented in Section 5, followed by conclusions in Section 6.

2. Model of the Battery

Lumped-Parameter Model of the Battery

An equivalent circuit model is developed on the basis of the dynamic features and operation mechanism of batteries [54]. The result indicates that 1RC and 2RC network-based lumped-parameter models of battery have good performance in terms of their estimation precision and model complexity [8]. In this paper, the 1RC network-based lumped-parameter model (Thevenin model) of battery, shown in Figure 1, is selected in consideration of calculation accuracy, computational and parameter identification complexities.

An equivalent circuit model has these components: the open circuit voltage U_{ocv} represents the voltage source and describes the static characteristic of the battery, an RC network consists of polarization resistance R_p and polarization capacitance C_p describes the polarization phenomenon of the battery, resistance R_0 represents the internal resistance of the battery.

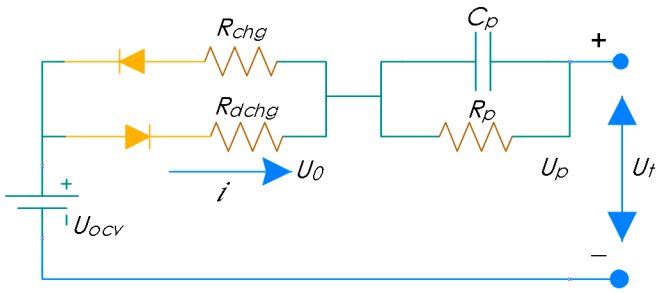

Figure 1. Model for a lithium-ion battery (LIB).

According to the analysis of the electric circuit [20], the electrical characteristics of the model of battery can be described as:

$$\dot{U}_p = -U_p/C_pR_p + i/C_p \tag{1}$$

$$U_t = U_{ocv} - U_p - U_0 \tag{2}$$

$$\begin{cases} U_0 = iR_{dchg} & (discharge) \\ U_0 = -iR_{chg} & (charge) \end{cases} \tag{3}$$

where the load current is represented with i (charge describes negative, discharge describes positive); the open-circuit voltage (OCV) is represented with U_{ocv}; U_t and U_p respectively denote the terminal voltage and the polarization voltage; R_p and C_p represent the polarization resistance and capacitance of the RC network, respectively; U_0 represents the internal resister voltage; R_{chg} and R_{dchg} denote the internal resistance when the battery is charging or discharging, respectively.

The SOC of a battery denotes the ratio of the remaining capacity to the total capacity. After the current integral and discretization, SOC can be obtained using the following equation:

$$\mathrm{SOC}(t) = \mathrm{SOC}(t_0) + (\eta \int_{t_0}^{t} i(t)dt)/C_N \tag{4}$$

where $\mathrm{SOC}(t)$ is the SOC of the battery at time (t), $\mathrm{SOC}(t_0)$ is the SOC of the battery at the previous point (t_0), η_k is the Coulomb efficiency, and C_N is the battery-rated capacity.

After the discretization of (2), we can obtain the following formula:

$$U_{p,k} - U_{p,k-1}/T_s = -U_{p,k-1}/C_pR_p + I_{k-1}/C_p \tag{5}$$

Subsequently, we can acquire the following formula:

$$U_{p,k} = (1 - T_s/C_pR_p)U_{p,k-1} + T_s/C_pI_{k-1} \tag{6}$$

where $U_{p,k}$ denotes the U_p at time (k), $U_{p,k-1}$ denotes the U_p at time $(k-1)$, T_s represents the sample time, and I_{k-1} represents the current at time $(k-1)$.

U_p and SOC are selected as system state variables, i is selected as an input variable, and U_t is selected as an output variable on the basis of Formulas (1)–(4) and (6). Then, the following formulas can be obtained:

$$\begin{pmatrix} U_{p,k} \\ \mathrm{SOC}_k \end{pmatrix} = \begin{pmatrix} (1 - T_s/C_pR_p) & 0 \\ 0 & 1 \end{pmatrix} \begin{pmatrix} U_{p,k-1} \\ \mathrm{SOC}_{k-1} \end{pmatrix} + \begin{pmatrix} T_s/C_p \\ \eta_k T_s/C_N \end{pmatrix} (I_{k-1}) + \begin{pmatrix} \omega_{1,k-1} \\ \omega_{2,k-2} \end{pmatrix} \tag{7}$$

$$\begin{cases} (U_{t,k}) = \begin{pmatrix} 1 \\ 0 \end{pmatrix}^T \begin{pmatrix} U_{P,k} \\ \mathrm{SOC}_k \end{pmatrix} + \left(R_{dchg}\right)(I_k) + U_{OCV} + (v_k) \quad (discharge) \\ (U_{t,k}) = \begin{pmatrix} 1 \\ 0 \end{pmatrix}^T \begin{pmatrix} U_{P,k} \\ \mathrm{SOC}_k \end{pmatrix} - \left(R_{chg}\right)(I_k) + U_{OCV} + (v_k) \quad (charge) \end{cases} \tag{8}$$

Formula (7) describes the state equation of the Thevenin model, and Formula (8) describes the observation equation of the Thevenin model. At time (k), I_k, $U_{t,k}$ and v_k denote the current, terminal voltage and measurement noise, respectively, and $\omega_{1,k-1}, \omega_{2,k-2}$ represent the process noise.

Define:

$$x_k = \begin{pmatrix} U_{p,k} \\ \mathrm{SOC}_k \end{pmatrix}, A_k = \begin{pmatrix} (1 - T_s/C_p R_p) & 0 \\ 0 & 1 \end{pmatrix}, B_k = \begin{pmatrix} T_s/C_p \\ \eta_k T_s/C_N \end{pmatrix}$$

The equation of time state is:

$$f(x_k, u_k) = A_k x_k + B_k I_k \tag{9}$$

With battery voltage as an output variable, we can generate the following observation equation:

$$\begin{array}{l} g(x_k, u_k) = U_{ocv} + U_{p,k} + R_{dchg} I_k \quad (discharge) \\ g(x_k, u_k) = U_{ocv} + U_{p,k} - R_{chg} I_k \quad (charge) \end{array} \tag{10}$$

3. Cubature Integral Approximation Method and SRCKF Algorithm

3.1. Cubature Using Numerical Integral Approximation Method

The numerical method of calculating cubature is introduced before elaborating the SRCKF algorithm, considering that SRCKF is based on the cubature integral approximation method. We take the n-dimensional integral of the following Gaussian density function [40]:

$$I(f) = \int_{R^n} f(x) \exp(-x^T x) dx \tag{11}$$

where $f(x)$ denotes an arbitrary function and R^n denotes the integral region. The key of the Bayesian theory to solve nonlinear Gaussian filtering is the integral of Formula (11). The integral term $f(x) \exp(-x^T x)$ can be summarized as multidimensional integrals with the form of "nonlinear function $\times$ Gaussian probability density".

We define $x = ry, y^T y = 1, r \in [0, \infty)$, and Formula (11) can be expressed as:

$$I(f) = \int_0^\infty \int_{U_n} f(ry) r^{n-1} \exp(-r^2) d\sigma(y) dr \tag{12}$$

$U_n = \left\{ y \in R^n \middle| y^T y = 1 \right\}$ is a supersphere with a radius of 1, and $\sigma(\cdot)$ is a spherical metric unit. Formula (12) can be simplified as

$$I(f) = \int_0^\infty S(r) r^{n-1} \exp(-r^2) dr \tag{13}$$

$$S(r) = \int_{U_n} f(ry) d\sigma(y) \tag{14}$$

Therefore, the n-dimensional integral Formula (11) can be transformed into a spherical radial integral form, as shown in Formulas (13) and (14). The spherical integral principle and the radial principle can be used to solve this equation.

$$\int_{U_n} f(y) d\sigma(y) \approx \omega \sum_{i=1}^{2n} f[u]_i \tag{15}$$

$$\int_a^b f(x)\omega(x)dx \approx \omega_i \sum_{i=1}^{m} f(x_i) \tag{16}$$

Formula (15) shows a third-order spherical integral structure under the spherical integral principle, and $[u]_i$ is the i element of the generated operator. Formula (16) presents the radial principle of the sphere, which means that m point Gaussian integral can be equivalent to the sum of $(2m-1)$ polynomials. $\omega(x)$ is a nonnegative weight function in the integral interval $[a, b]$.

SRCKF uses the spherical radial principle to select $2n$ (n is state dimension) with corresponding weight point set (ω_i, ζ_i), which can be used to approximate the posterior mean value and covariance of the nonlinear state.

$$I(f) = \sum_{i=1}^{m} \omega_i f(\zeta_i) \tag{17}$$

$$\begin{cases} \zeta_i = \sqrt{n}[1]_i, \\ \omega i = \frac{1}{2n}, \\ i = 1, 2, \ldots, 2n. \end{cases} \tag{18}$$

where $[1]_i$ represents the column i of set $[1]$. We define $n = 2$ and obtain

$$[1] = \left\{ [1,0]^T, [0,1]^T, [-1,0]^T, [0,-1]^T \right\} \tag{19}$$

3.2. SRCKF Algorithm

We define n-dimensional nonlinear discrete-state space mode and acquire

$$x_k = f(x_{k-1}, u_{k-1}) + \omega_{k-1}, k = 0, 1, \cdots \tag{20}$$

$$z_k = h(x_k, u_k) + v_k, k = 0, 1, \cdots \tag{21}$$

where u_k is the known input, ω_{k-1} is the system noise, and v_k is the noise of measurement.

The following three steps describe the SRCKF algorithm:

Step 1. Initialization of state estimation. We set the initial value of state to $\hat{x}_{0|0}$ and obtain

$$\begin{cases} \hat{x}_{0|0} = E(x_0) \\ S_{0|0} = chol\left(E\left[(x_0 - \hat{x}_{0|0})(x_0 - \hat{x}_{0|0})^T\right]\right) \end{cases} \tag{22}$$

where $U = chol(A)$ is the Cholesky decomposition of matrix A, $A = U^T U$, U is the upper triangular matrix, and $E(\cdot)$ is the expectation.

Step 2. State prediction ($k = 1, 2, 3, \cdots$).

Step 2.1 n cubature points for battery states at time $k-1$ ($i = 1,\ 2, \cdots,\ 2n$) are calculated.

$$X_{i,k-1|k-1} = S_{k-1|k-1}\xi_i + \hat{x}_{k-1|k-1} \tag{23}$$

Step 2.2: The battery state Formula (7) is used to propagate cubature points and generate new points.

$$X^*{}_{i,k|k-1} = f(X_{i,k-1|k-1}, u_{k-1}) \tag{24}$$

Step 2.3: After the newly generated points are weighted, the sum of the weighted points is determined and then the prediction value of the battery state at time k can be estimated (SRCKF uses equal weights).

$$\hat{x}_{k|k-1} = 1/2n \sum_{i=1}^{2n} X^*{}_{i,k|k-1} \tag{25}$$

Step 2.4: The square root of the covariance matrix of the prediction value is estimated.

$$S_{k|k-1} = Tria\left(\left[\chi^*{}_{k|k-1} S_{Q,k-1}\right]\right) \tag{26}$$

where $Q_{k-1} = S_{Q,k-1} S_{Q,k-1}^T$.

$$\chi^*{}_{k|k-1} = 1/\sqrt{2n}\left[X^*{}_{1,k-1} - \hat{x}_{k|k-1}, X^*{}_{2,k-1} - \hat{x}_{k|k-1}, \cdots, X^*{}_{2n,k-1} - \hat{x}_{k|k-1}\right] \tag{27}$$

$S = Tria(A)$ represents the QR decomposition of matrix A, which obtains a normal orthogonal matrix B and an upper triangular matrix C. We define $S = C^T$, and S is the upper triangular matrix.

Step 3. Measurement update.

After the state prediction value of time k is obtained, the prediction value can be updated with the observation value at this moment to obtain the optimal state estimation value.

Step 3.1: A set of equal-weight cubature points by the square root matrix of the state prediction value and its covariance matrix is generated using the spherical radial rule ($i = 1,\ 2, \cdots,\ 2n$).

$$X_{i,k|k-1} = S_{k|k-1}\xi_i + \hat{x}_{k|k-1} \tag{28}$$

Step 3.2: The battery observation Formula (8) is used to propagate the cubature points.

$$Z_{i,k|k-1} = h\left(X_{i,k|k-1}, u_k\right) \tag{29}$$

Step 3.3: The prediction value of observation at time k is generated.

$$\hat{z}_{k|k-1} = 1/2n \sum_{i=1}^{2n} Z_{i,k|k-1} \tag{30}$$

Step 3.4: The square root of the covariance matrix of the estimated prediction value of observation is estimated.

$$S_{zz,k|k-1} = Tria\left(\left[Z_{k|k-1} \quad S_{R,k}\right]\right) \tag{31}$$

where $Rk = S_{R.k} S_{R,k}^T$, and

$$Z_{k|k-1} = 1/\sqrt{2n}\left[Z_{1,k|k-1} - \hat{z}_{k|k-1}, Z_{2,k|k-1} - \hat{z}_{k|k-1}, \cdots, Z_{2n,k|k-1} - \hat{z}_{k|k-1}\right] \tag{32}$$

Step 3.5: The observation and prediction values of the square root of the covariance matrix of each other are estimated.

$$P_{xz,k|k-1} = \chi_{k|k-1} Z_{k|k-1}^T \tag{33}$$

where

$$\chi_{k|k-1} = 1/\sqrt{2n}\left[X_{1,k|k-1} - \hat{x}_{k|k-1}, X_{2,k|k-1} - \hat{x}_{k|k-1}, \cdots, X_{2n,k|k-1} - \hat{x}_{k|k-1}\right] \tag{34}$$

Step 3.6: The SRCKF filter gain matrix is solved.

$$W_k = \left(P_{xz,k|k-1} / S_{zz,k|k-1}^T\right) / S_{zz,k|k-1} \tag{35}$$

Step 3.7: The best state value estimate of the battery at time k is calculated.

$$\hat{x}_{k|k} = \hat{x}_{k|k-1} + W_k\left(z_k - \hat{z}_{k|k-1}\right) \tag{36}$$

Step 3.8: The square root of the error covariance matrix of the optimal state estimation of the battery at time k is calculated.

$$S_{k|k} = Tria\left(\left[\chi_{k|k-1} - W_k Z_{k|k-1} \quad W_k S_{R,k}\right]\right) \tag{37}$$

After the value of the state estimation $\hat{x}_{k|k}$ and its covariance square root $S_{k|k}$ are obtained at time k, Step 2 is repeated at time $k+1$, and the next iteration is performed. Flowchart of the method using SRCKF is shown in Figure 2.

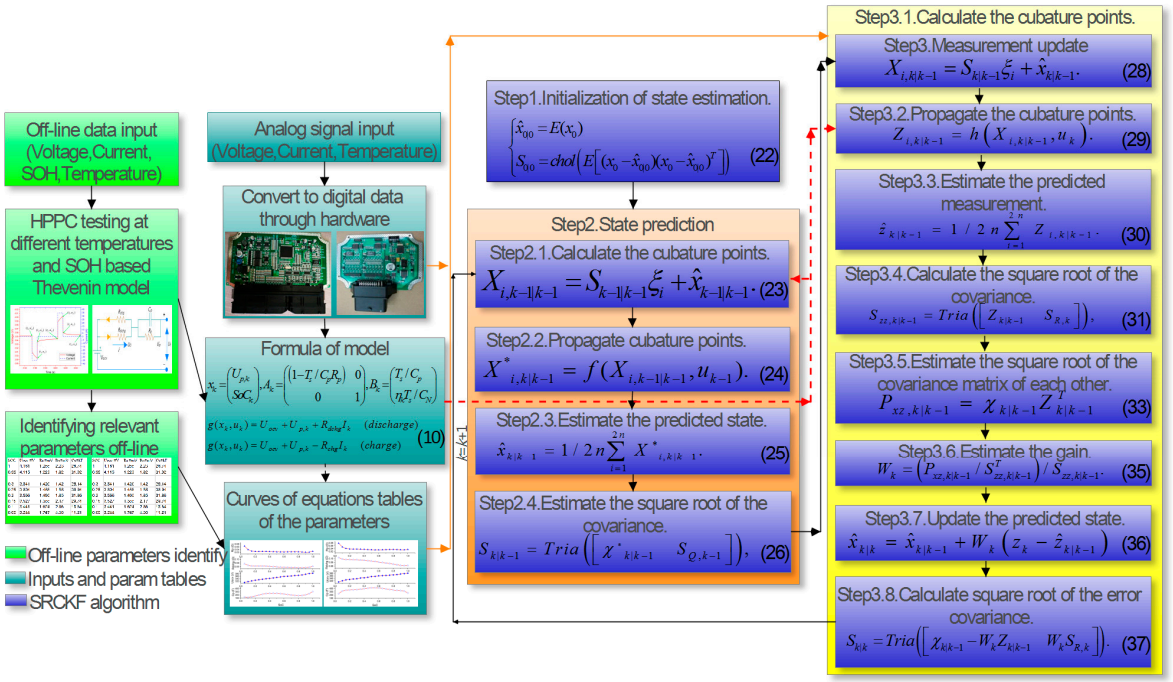

Figure 2. Flowchart of the method using square root cubature Kalman filter (SRCKF).

4. Experimental Configurations, HPPC Test and Off-Line Identification of Relevant Parameters

According to the algorithm model, a test bench for the cells was built, which included cells of the battery, charging and discharging equipment (NBT BTS5200C4, Newaresles Limited, Shenzhen, China), monitoring platform, environment oven, testing cable, the hardware of the battery management unit (BMU) and local electronic control unit (LECU), and communication cables. The test bench can not only conduct Hybrid pulse power characterization (HPPC) tests to identify the relevant parameters of the battery off-line but also it can be used for simulation and verification according to the condition of a real environment.

HPPC tests must be conducted at various temperatures and different state of health (SOH) to identify the parameters of U_{ocv}, $R_{dchg}(R_{chg})$, C_p, R_p, and SOC and input them into the table to be used by the SRCKF algorithm to meet the requirements of the vehicle at various temperatures (-20 °C to 55 °C every 5 °C) and SOH (1 to 0.8 every 0.05). The specifications of the battery cell are shown in Table 1, the test equipment specifications are shown in Table 2, and Figure 3 shows the configuration of the battery test bench.

Table 1. Specifications of the battery cell.

Item	Value
Cell Voltage	3.7 V
Cell Capacity	35 Ah
Maximum charging rates	2 C
Maximum discharging rates	4 C

Table 2. Specifications of the NBT BTS5200C4.

Item	Value
Max value of discharging current	200 A
Max value of charging current	200 A
Range of voltage measurement	0~5 V
Current measurement error	0.1%F.S. but not better than ±20 mA
Voltage measurement error	0.1%F.S. but not better than ±20 mV
Temperature measurement error	±1 °C

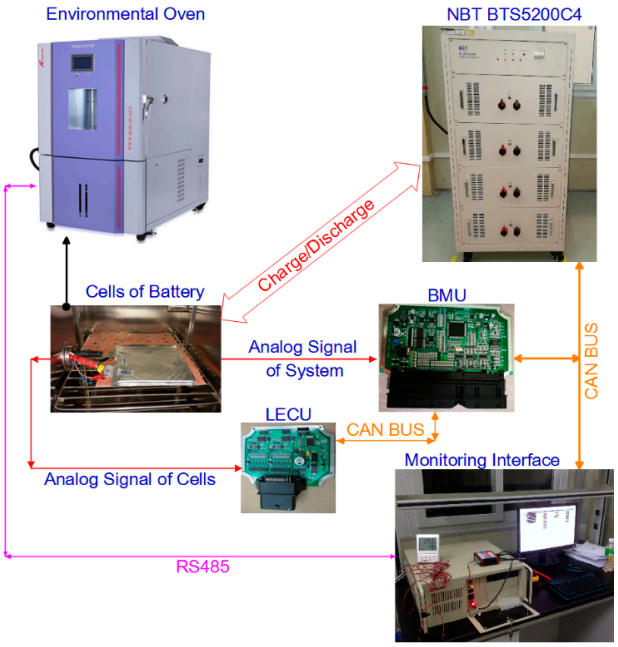

Figure 3. Configuration of the battery cell test bench.

It is noted that, because of the high accuracy of NBT BTS5200C4, the reference values of SOC can be acquired by the current integral method with the measured value. To get a precise initial SOC, the battery cell is fully charged before test with a constant current, firstly. And to obtain an accurate terminal SOC, the battery cell is fully discharged after test, finally.

The HPPC test cycle of the battery cell is shown in Figure 4. There are various methods to fit functions in the MATLAB (R2016b, The MathWorks, Inc., Natick, MA, USA) simulation environment, such as polyfit command, is curvefit command, and cftool [55]. Among these methods, cftool is chosen to fit functions in this study, because it provides a visual graphical interface and powerful curve-fitting ability. The least square method [56] is used on the basis of the Formulas (1) and (2) to identify unknown parameters. The fitting curves of $U_{ocv}, R_{dchg}, C_p, R_p$, and SOC equations are provided in Figure 5 (Temperature = 25 °C, SOH = 1) and Figure 6 (Temperature = 15 °C, SOH = 0.9). The coefficients of the corresponding equation ($y = f(x) = ax^6 + bx^5 + cx^4 + dx^3 + ex^2 + fx^1 + g$) are indicated in Tables 3 and 4.

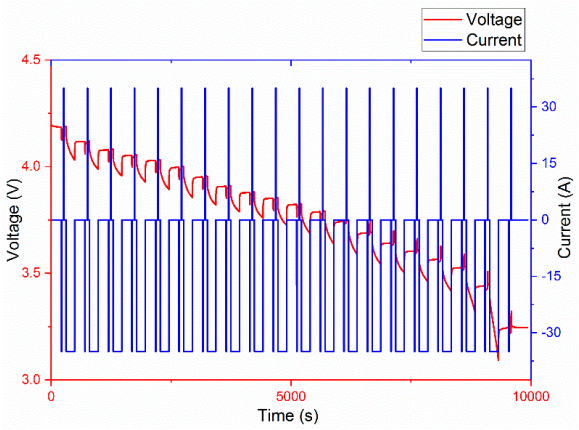

Figure 4. Hybrid pulse power characterization (HPPC) test cycle of the battery (at 1 C).

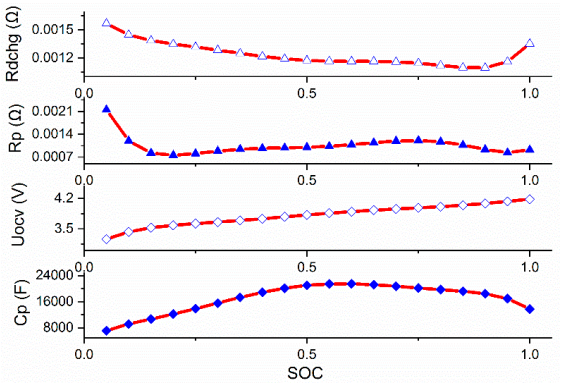

Figure 5. Relationship between state of change (SOC) and $U_{ocv}, R_{dchg}, C_p, R_p$ (temperature = 25 °C, state of health (SOH) = 1).

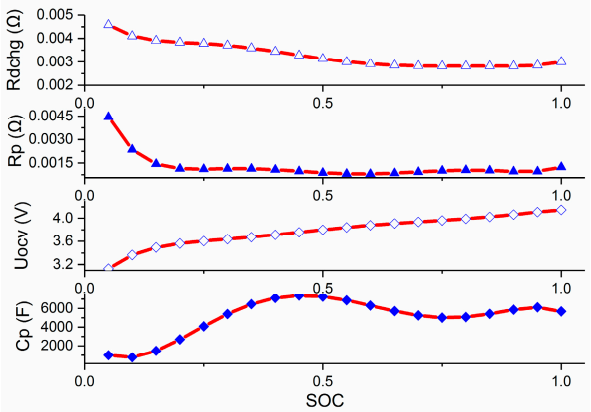

Figure 6. Relationship between SOC and $U_{ocv}, R_{dchg}, C_p, R_p$ (temperature = 15 °C, SOH = 0.95).

Table 3. Equation coefficients at temperatures = 25 °C and SOH = 1.

Coefficients	g	f	e	d	c	b	a
R_p	0.004107	−0.052842	0.316150	−0.917690	1.395537	−1.062447	0.318105
R_{dchg}	0.001812	−0.006602	0.041589	−0.144026	0.258410	−0.226639	0.076809
U_{ocv}	2.971124	7.396502	−37.015633	101.27299	−143.46866	100.40782	−27.381834
C_p	3839	86,475	−502,083	2,080,696	−4,107,296	3,696,315	−1,244,161

Table 4. Equation coefficients at temperatures = 15 °C and SOH = 0.95.

Coefficients	g	f	e	d	c	b	a
R_p	0.008551	−0.108954	0.621934	−1.758040	2.593975	−1.910763	0.554538
R_{dchg}	0.005575	−0.027267	0.171668	−0.538437	0.840745	−0.636656	0.187370
U_{ocv}	2.712023	10.728256	−55.006330	149.858773	−213.2116	151.254438	−42.189757
C_p	2677	−51,640	397,937	−773,697	312,761	400,225	−282,581

5. Results and Discussion

Under the same conditions, three different experiments were performed to test the performance of the proposed algorithm: constant current discharge test, dynamic stress test (DST), and DST test with noise measurement. At a temperature of 25 °C and SOH = 1, by using Figure 3 as the test bench, and the results of the battery parameters shown in Table 2, the EKF, UKF, CKF, and SRCKF algorithms were compared in the experiment. The comparison results were given in the performances of estimation accuracy, convergence speed, robustness, and calculation cost. Moreover, under real conditions, the actual current and voltage showed deviation from measured results due to the measurement errors of the voltage and current sensors and interference of corresponding hardware circuits (such as EMI). To verify the proposed algorithm robustness against the noise of measurement, a random interference to the system was conducted. Simulations of 100 cycles of the four algorithms were run in the Intel Core i7-4600U (2.1 GHz, 2.7 GHz, Intel Corporation, Santa Clara, CA, USA) to obtain the calculation cost of the algorithms. The test results are shown in Table 5. The comparison results showed that the proposed method had lesser computation cost than the other methods. Hence, because of the difference of calculation cost of the four algorithms, a cycle of the algorithms was run every 100 ms with BMU to ensure that the cycle was fully completed.

Table 5. Simulation results of the calculation cost.

Methods	EKF	UKF	CKF	SRCKF
Computation cost (s)	0.0023	0.01788	0.006775	0.00774

5.1. Experiment A: Test with Constant Discharge Current

In this experiment, with a constant current of 34.95 A (approximately 1 C), the cell of the battery was discharged from the initial state (SOC = 1) to the final state (SOC = 0.00027). The voltage of terminal decreased from 4.14 V to 2.5105 V. The curve of the test is shown in Figure 7. The current of the battery is constant with the car running in a constant speed. Thus, this experiment can be used to simulate this condition. The experimental results of convergence speed are shown in Figure 8. The cyan line is the reference value of SOC calculated by the BTS5200C4 with a precise initial value of SOC, and the estimated SOC is described with the red line. The initial value of real SOC is 1, and the estimated one is 0.5. A comparison of results from the EKF, UKF, CKF, and SRCKF estimation algorithms are shown in Figure 8a–d, respectively. Figure 9 shows the estimation SOC errors of the EKF, UKF, CKF, and SRCKF estimation algorithms, and the results of probability of estimation SOC errors are shown in Figure 10. Table 6 shows the data of the root mean square errors (RMSE), mean errors, maximum errors, and convergence time. The estimation SOC errors of the EKF, UKF, CKF, and SRCKF estimation algorithms are shown in Figure 9a–d, respectively. Similarly, the results of the probability of estimation SOC errors of the EKF, UKF, CKF, and SRCKF estimation algorithms are shown in Figure 10a–d, respectively. From the experiment results of Experiment A, the following conclusions are obtained. Under constant current discharge, (1) the proposed method had a faster convergence rate in the case of a higher accuracy of SOC estimation than the other three methods; (2) the estimation SOC error of the proposed method was distributed in the small region near zero, which showed good stability

of the SRCKF algorithm; and (3) the proposed method met the requirement of the constant current discharge condition.

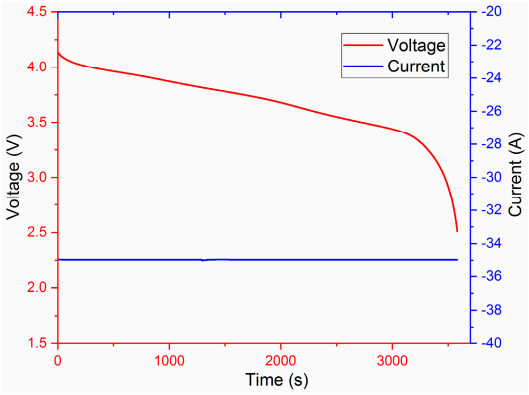

Figure 7. Test with constant discharge current using battery cell.

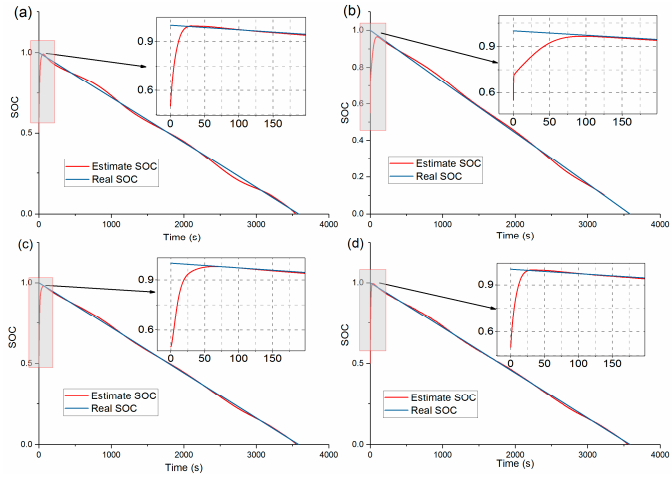

Figure 8. Results of the convergence speed in experiment A: (**a**) EKF, (**b**) UKF, (**c**) CKF, (**d**) SRCKF.

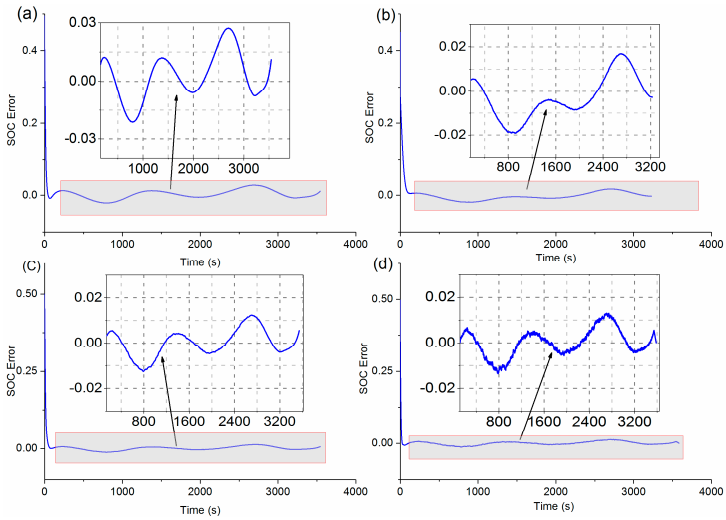

Figure 9. Results of SOC errors in experiment A: (**a**) EKF, (**b**) UKF, (**c**) CKF, (**d**) SRCKF.

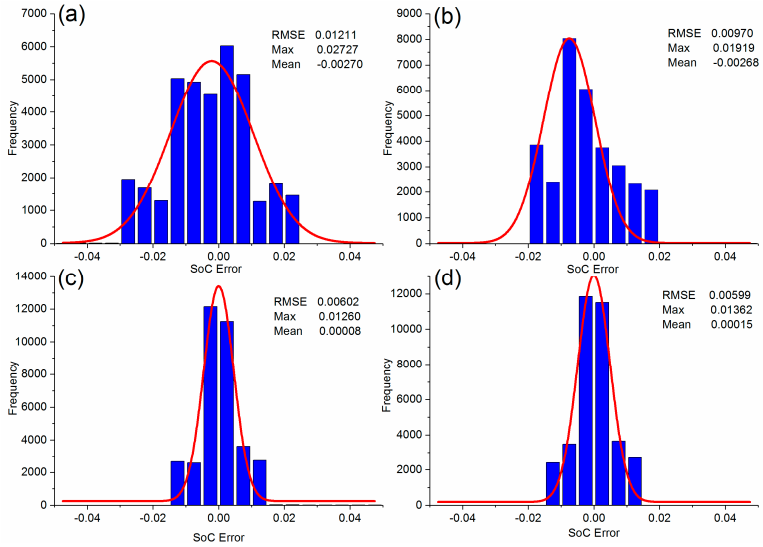

Figure 10. Results of the probability of SOC errors in experiment A: (**a**) EKF, (**b**) UKF, (**c**) CKF, (**d**) SRCKF.

Table 6. Experimental results of Experiment A.

Methods	Convergence Time (s)	RMSE	Max Error	Mean Error
EKF	25	0.01211	0.02727	0.00270
UKF	110	0.00970	0.01701	−0.00268
CKF	60	0.00602	0.01233	0.00008
SRCKF	25	0.00599	0.01308	0.00015

5.2. Experiment B: DST

The DST is simplified from actual urban driving cycles (AUDC). The current of battery with the DST in Experiment B is shown in Figure 11, with battery charge denoted with the positive current and battery discharge denoted with the negative current. Figure 11a shows one test cycle of DST and Figure 11b shows 20 test cycles of DST that were used in Experiment B. Experimental results of the convergence speed are shown in Figure 12. The cyan line is the reference value of SOC calculated by the BTS5200C4 with a precise initial value of SOC, and the estimated SOC is plotted by the red line. The initial value of real SOC was 1, and the estimated one was 0.5. The results of the EKF, UKF, CKF, and SRCKF estimation algorithms are shown in Figure 12a–d, respectively. To maintain proper estimation accuracy and convergence speed, the parameters of the EKF were adjusted to avoid the divergence of the EKF algorithm in Experiment B. However, the EKF algorithm still had the problem of divergence and filtering interruption in Experiment B. The curve in the purple circles represents this problem in Figure 12a. Figure 13 shows the estimation SOC errors of the EKF, UKF, CKF, and SRCKF estimation algorithms, and the results of probability of estimation SOC errors are shown in Figure 14. Table 7 shows the data of the root mean square errors (RMSE), mean errors, maximum errors, and convergence time. In comparison with Experiment A, the accuracy of the SOC estimation of the EKF, UKF, CKF, and SRCKF estimation algorithms decreases because the voltage and current have strong nonlinear changes. At the same time, because of the adjustment of the parameters of the EKF algorithm, the convergence speed time is long. Hence, the following conclusions are obtained from Experiment B. Under the DST condition, (1) the SRCKF algorithm had a faster convergence rate and better accuracy of SOC estimation than the other three methods; (2) the estimation error of the SRCKF algorithm was distributed in the small region near zero, which showed the good stability of the SRCKF algorithm; (3) the SRCKF algorithm met the requirement of the DST condition.

Table 7. Experimental results of Experiment B.

Methods	Convergence Time (s)	RMSE	Max Error	Mean Error
EKF	65	0.01560	0.05064	−0.01443
UKF	85	0.00864	0.03058	−0.01047
CKF	60	0.00912	0.02665	−0.00705
SRCKF	25	0.00892	0.02469	−0.00704

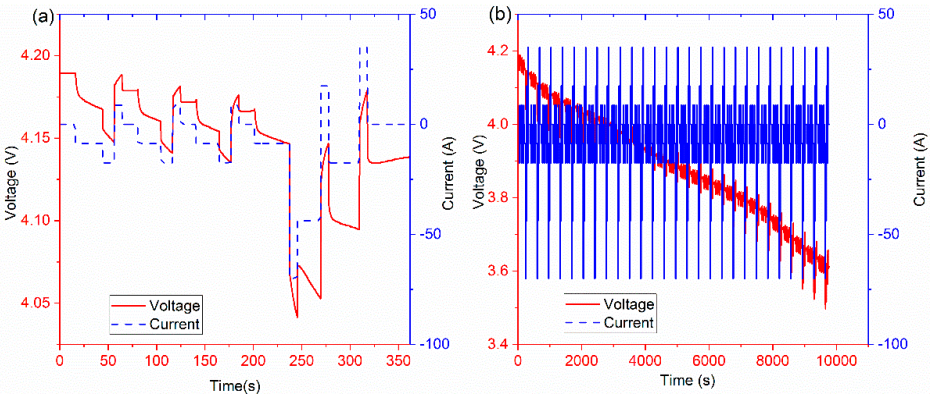

Figure 11. Dynamic stress test (DST) of the battery: (**a**) One test cycle; (**b**) 20 test cycles.

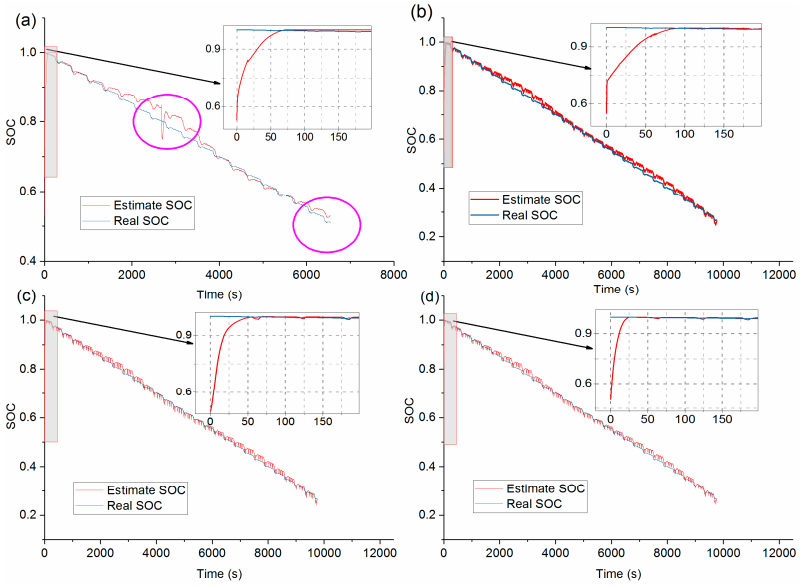

Figure 12. Results of the convergence speed in Experiment B: (**a**) EKF, (**b**) UKF, (**c**) CKF, (**d**) SRCKF.

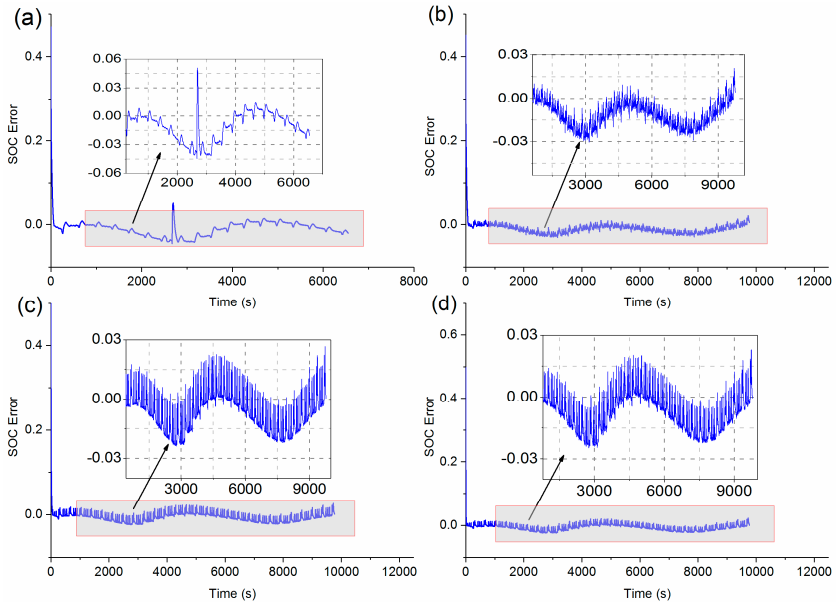

Figure 13. Results of SOC errors in Experiment B: (**a**) EKF, (**b**) UKF, (**c**) CKF, (**d**) SRCKF.

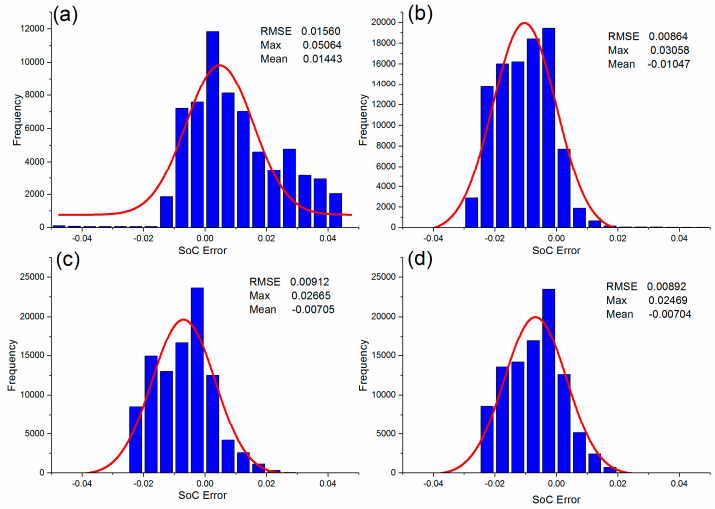

Figure 14. Results of the probability of SOC errors in Experiment B: (**a**) EKF, (**b**) UKF, (**c**) CKF, (**d**) SRCKF.

5.3. Experiment C: DST with Noise Measurement

In Experiment C, the conditions were the same as Experiment B, as shown in Figure 11. To verify the robustness of the proposed algorithm against the voltage and current errors, stochastic normal distributed noises were added to the measurement voltage and current. The standard deviation of the noise was calculated as follows:

$$\theta = \alpha N_{\max}/3 \tag{38}$$

where θ denotes the arithmetic mean, α denotes a scaling factor, and $N_{\max}$ denotes the maximum voltage or the maximum current. Conditions of α = 1%, 2.5%, 5% are studied in this paper. The results of the current and voltage in Experiment C, with both voltage and current noises, are shown in Figure 15. Similar to Experiment B, the initial value of real SOC was 1, and the estimated one was 0.5. Because of the noise, the methods of EKF, UKF, and CKF diverged. The filters were interrupted in approximately 120 s. The curve in blue circle represents this problem in Figure 16. Evidently, the proposed method worked well. Hence, the RMSEs, mean errors, maximum errors, and convergence time of EKF, UKF,

and CKF were not obtained in Experiment C. They were obtained in the SRCKF method with the different noises. The results are shown in Table 8, and the results of the probability of the corresponding estimation SOC errors are shown in Figure 17. In the real EVS, the error of current and voltage was not more than 2.5% after the signals were filtered through the hardware and software. As shown in Table 8, in the case of error $\leq$2.5%, the proposed method still maintained a high estimation accuracy, and its RMSEs and mean error values were still small enough to be applied to the actual EVS. Although the maximum error of the estimation SOC was bound within 8%, the RMSEs and mean errors of the proposed method were still small. From the point of error distribution shown in Figure 17d, the majority of the error distribution is within 5%. The conclusions of Experiment C, in the DST condition with noise ($\geq$1%), are the following: (1) The proposed method had a faster convergence rate (approximately 25 s) and better accuracy of estimation SOC with noise than the other three methods; (2) the estimation error of the SRCKF algorithm was distributed in the small region near zero, which showed the good stability of the proposed method; (3) the proposed method had a weaker robustness against the disturbance than the methods of EK, UKF, and CKF and met the requirement of the DST condition with noises.

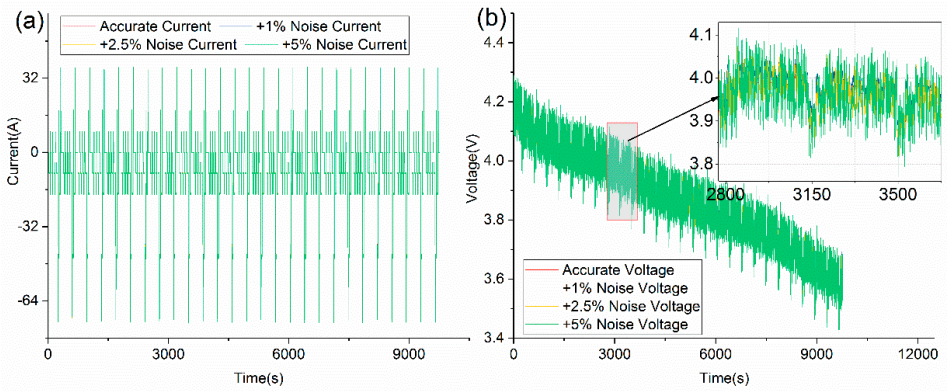

Figure 15. Results of the current and voltage with noise in Experiment C: (**a**) current, (**b**) voltage.

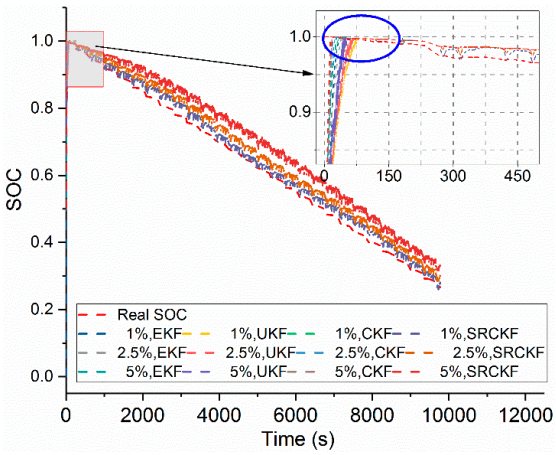

Figure 16. Results of SOC estimation in Experiment C.

Table 8. Experimental results of Experiment C with the proposed method.

SRCKF	RMSE	Max Error	Mean Error
1% noise	0.01081	0.03489	−0.00273
2.5% noise	0.01693	0.05347	0.00055
5% noise	0.02004	0.07971	0.00279

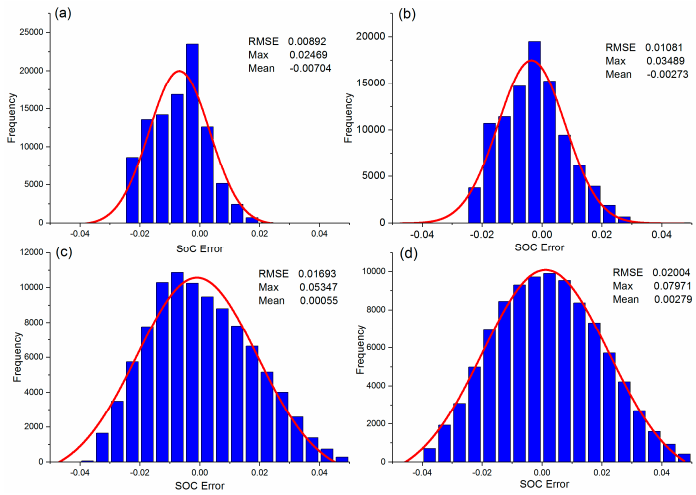

Figure 17. Results of the probability of SOC errors with the proposed method in Experiment C: (**a**) no noise, (**b**) 1% noise, (**c**) 2.5% noise, (**d**) 5% noise.

6. Conclusions

In this paper, a new SOC estimation method using the SRCKF algorithm is proposed to simultaneously improve the SOC estimation accuracy and reduce the computation cost. Under strong nonlinear working conditions, filtering divergence can be avoided. Some findings from the present study are summarized as follows.

(1) The shortcomings of several common algorithms for battery SOC are investigated, and the SRCKF algorithm is recommended for its accuracy and speed. To balance between model accuracy and computation cost, the Thevenin model was applied to simulate the dynamic characteristics of the LIB, based on which Equations (9) and (10) were derived. With this model, experimental and parameter identification methods for off-line identification of battery parameters were proposed, and four Simulink algorithm models were established according to the EKF, UKF, CKF, and SRCKF algorithms, respectively.

(2) Constant current discharge tests and DST cycles were conducted to verify the performance of the proposed method against other three methods (i.e., EKF, UKF, and CKF). The results of experiments showed that the estimation SOC error with the proposed method quickly converged to 2% within approximately 25 s, whereas the initial SOC error reached 50%. The RMSEs (0.00892), maximum error (0.02469), and mean error (−0.00704) of the proposed method were the best among all the methods in DST. Moreover, the maximum error was less than 5.5% even when the measurement noise of the voltage and the current was up to 2.5% in DST with noise.

(3) Given the insufficient sensor accuracy and inaccurate hardware circuit, the signal of voltage and current are often interfered. Hence, a real EV running in a complex working condition (such as DST) with noises is very important. The method should be able to handle the nonlinear changes and random disturbance. In comparison with other methods (EKF, UKF, and CKF), only the proposed method avoided the filtering divergence in DST with noise (up to 5%).

Therefore, the proposed method ensured the robustness and estimation accuracy of the algorithm in the case of limited computing resource requirements and can be applied to new BMS with online SOC estimation easily. In the future, a new BMS with the proposed method to achieve good performance can be developed.

Acknowledgments: This work was sponsored by China's National "863" Project of the Twelfth Five-year Plan "Research and industrialization of pure electric vehicles" (No. 2011AA11A215). The authors would also like to thank the Wuhan University of Technology for the support.

Author Contributions: Xiangyu Cui planned the initial aide. Xiangyu Cui and Yazhou Guo designed the algorithm. Xiangyu Cui analyzed the experimental date and wrote the original manuscript. Maji Luo and Zhu Jing and Huimin Qiao established the experiment bench. Xiangyu Cui and Zhu Jing and Maji Luo revised the final manuscript.

Conflicts of Interest: The authors declare no conflict of interest.

Nomenclature

i	load current
U_{ocv}	open-circuit voltage
U_t	terminal voltage
U_p	polarization voltage
R_p	polarization resistance
C_p	polarization capacitance
U_0	internal resister voltage
R_{chg}	internal resistance when discharging
R_{dchg}	internal resistance when discharging
R^n	integral region
u_k	known input
$E(\cdot)$	expectation
N_{max}	max voltage or the max current

Greek Symbol

$\sigma(\cdot)$	spherical metric unit
$\omega(x)$	nonnegative weight function
(ω_i,ζ_i)	weight point set
ω_{k-1}	system noise
ν_k	noise of measurement
θ	arithmetic mean
α	scaling factor

Acronyms and Abbreviations

OCV	open-circuit voltage
SOC	state of charge
SRCKF	square root cubature Kalman filter
EKF	Extended Kalman filter
UKF	unscented Kalman filter
CKF	cubature Kalman filter
EV	electric vehicle
LIB	lithium-ion battery
BMS	battery management system
PF	particle filter
UT	unscented transform
LECU	local electronic control unit
BMU	battery management unit
HPPC	hybrid pulse power characteristic
SOH	state of health
DST	dynamic stress test
EMI	electromagnetic interference
RMSE	root mean square error
Ah	ampere-hour
C	discharge rate
MATLAB	MATrix LABoratory

References

1. Chong, U.; Yim, S.H.L.; Barrett, S.R.H.; Boies, A.M. Air quality and climate impacts of alternative bus technologies in greater London. *Environ. Sci. Technol.* **2014**, *48*, 4613–4622. [CrossRef] [PubMed]
2. Remmlinger, J.; Buchholz, M.; Meiler, M.; Bernreuter, P.; Dietmayer, K. State-of-health monitoring of lithium-ion batteries in electric vehicles by on-board internal resistance estimation. *J. Power Source* **2011**, *196*, 5357–5363. [CrossRef]
3. Gerssen-Gondelach, S.J.; Faaij, A.P.C. Performance of batteries for electric vehicles on short and longer term. *J. Power Source* **2012**, *212*, 111–129. [CrossRef]
4. Lu, L.; Han, X.; Li, J.; Hua, J.; Ouyang, M. A review on the key issues for lithium-ion battery management in electric vehicles. *J. Power Source* **2013**, *226*, 272–288. [CrossRef]
5. Xiong, R.; Sun, F.; Gong, X.; He, H. Adaptive state of charge estimator for lithium-ion cells series battery pack in electric vehicles. *J. Power Source* **2013**, *242*, 699–713. [CrossRef]
6. Adany, R.; Aurbach, D.; Kraus, S. Switching algorithms for extending battery life in Electric Vehicles. *J. Power Source* **2013**, *231*, 50–59. [CrossRef]
7. Li, J.; Klee Barillas, J.; Guenther, C.; Danzer, M.A. Multicell state estimation using variation based sequential Monte Carlo filter for automotive battery packs. *J. Power Source* **2015**, *277*, 95–103. [CrossRef]
8. Sun, F.; Xiong, R.; He, H. A systematic state-of-charge estimation framework for multi-cell battery pack in electric vehicles using bias correction technique. *Appl. Energy* **2016**, *162*, 1399–1409. [CrossRef]
9. Zhong, L.; Zhang, C.; He, Y.; Chen, Z. A method for the estimation of the battery pack state of charge based on in-pack cells uniformity analysis. *Appl. Energy* **2014**, *113*, 558–564. [CrossRef]
10. Xiong, R.; Sun, F.; He, H.; Nguyen, T.D. A data-driven adaptive state of charge and power capability joint estimator of lithium-ion polymer battery used in electric vehicles. *Energy* **2013**, *63*, 295–308. [CrossRef]
11. Fathabadi, H. A novel design including cooling media for Lithium-ion batteries pack used in hybrid and electric vehicles. *J. Power Source* **2014**, *245*, 495–500. [CrossRef]
12. Hooper, J.M.; Marco, J. Characterising the in-vehicle vibration inputs to the high voltage battery of an electric vehicle. *J. Power Source* **2014**, *245*, 510–519. [CrossRef]
13. Waag, W.; Fleischer, C.; Sauer, D.U. Critical review of the methods for monitoring of lithium-ion batteries in electric and hybrid vehicles. *J. Power Source* **2014**, *258*, 321–339. [CrossRef]
14. Panchal, S.; Dincer, I.; Agelin-Chaab, M.; Fraser, R.; Fowler, M. Experimental and simulated temperature variations in a $LiFePO_4$ -20 Ah battery during discharge process. *Appl. Energy* **2016**, *180*, 504–515. [CrossRef]
15. Panchal, S.; McGrory, J.; Kong, J.; Dincer, I.; Agelin-Chaab, M.; Fraser, R.; Fowler, M. Cycling degradation testing and analysis of a LiFePO4 battery at actual conditions. *Willey Int. J. Energy Res.* **2017**, *41*, 2565–2575. [CrossRef]
16. Unterrieder, C.; Zhang, C.; Lunglmayr, M.; Priewasser, R.; Marsili, S.; Huemer, M. Battery state-of-charge estimation using approximate least squares. *J. Power Source* **2015**, *278*, 274–286. [CrossRef]
17. Hu, C.; Youn, B.D.; Chung, J. A multiscale framework with extended Kalman filter for lithium-ion battery SOC and capacity estimation. *Appl. Energy* **2012**, *92*, 694–704. [CrossRef]
18. Hung, M.-H.; Lin, C.-H.; Lee, L.-C.; Wang, C.-M. State-of-charge and state-of-health estimation for lithium-ion batteries based on dynamic impedance technique. *J. Power Source* **2014**, *268*, 861–873. [CrossRef]
19. Xiong, R.; Gong, X.; Mi, C.C.; Sun, F. A robust state-of-charge estimator for multiple types of lithium-ion batteries using adaptive extended Kalman filter. *J. Power Source* **2013**, *243*, 805–816. [CrossRef]
20. Ng, K.S.; Moo, C.-S.; Chen, Y.-P.; Hsieh, Y.-C. Enhanced coulomb counting method for estimating state-of-charge and state-of-health of lithium-ion batteries. *Appl. Energy* **2009**, *86*, 1506–1511. [CrossRef]
21. Xing, Y.; He, W.; Pecht, M.; Tsui, K.L. State of charge estimation of lithium-ion batteries using the open-circuit voltage at various ambient temperatures. *Appl. Energy* **2014**, *113*, 106–115. [CrossRef]
22. Kim, J.; Lee, S.; Cho, B.H. Discrimination of Li-ion batteries based on Hamming network using discharging–charging voltage pattern recognition for improved state-of-charge estimation. *J. Power Source* **2011**, *196*, 2227–2240. [CrossRef]
23. Wang, Y.; Zhang, C.; Chen, Z. A method for joint estimation of state-of-charge and available energy of $LiFePO_4$ batteries. *Appl. Energy* **2014**, *135*, 81–87. [CrossRef]
24. He, Y.; Liu, X.; Zhang, C.; Chen, Z. A new model for State-of-Charge (SOC) estimation for high-power Li-ion batteries. *Appl. Energy* **2013**, *101*, 808–814. [CrossRef]

25. Liu, X.; Chen, Z.; Zhang, C.; Wu, J. A novel temperature-compensated model for power Li-ion batteries with dual-particle-filter state of charge estimation. *Appl. Energy* **2014**, *123*, 263–272. [CrossRef]
26. Arulampalam, M.S.; Maskell, S.; Gordon, N.; Clapp, T. A tutorial on particle filters for online nonlinear/non-Gaussian Bayesian tracking. *IEEE Trans. Signal Process.* **2001**, *50*, 174–188. [CrossRef]
27. Djuric, P.M.; Kotecha, J.H.; Zhang, J.; Huang, Y.; Ghirmai, T.; Bugallo, M.F.; Miguez, J. Particle filtering. *IEEE Signal Process. Mag.* **2003**, *20*, 19–38. [CrossRef]
28. Kotecha, J.H.; Djuric, P.M. Gaussian particle filtering. *IEEE Trans. Signal Process.* **2003**, *51*, 2592–2601. [CrossRef]
29. Kotecha, J.H.; Djuric, P.M. Gaussian sum particle filtering. *IEEE Trans. Signal Process.* **2003**, *51*, 2602–2612. [CrossRef]
30. Schwunk, S.; Armbruster, N.; Straub, S.; Kehl, J.; Vetter, M. Particle filter for state of charge and state of health estimation for lithium–iron phosphate batteries. *J. Power Source* **2013**, *239*, 705–710. [CrossRef]
31. Plett, G.L. Extended Kalman filtering for battery management systems of LiPB-based HEV battery packs: Part 1. *J. Power Source* **2004**, *134*, 252–261. [CrossRef]
32. Plett, G.L. Extended Kalman filtering for battery management systems of LiPB-based HEV battery packs: Part 2. *J. Power Source* **2004**, *134*, 62–276. [CrossRef]
33. Plett, G.L. Extended Kalman filtering for battery management systems of LiPB-based HEV battery packs: Part 3. *J. Power Source* **2004**, *134*, 277–292. [CrossRef]
34. Wang, Y.; Zhang, C.; Chen, Z. A method for state-of-charge estimation of Li-ion batteries based on multi-model switching strategy. *Appl. Energy* **2015**, *137*, 427–434. [CrossRef]
35. Xiong, R.; Sun, F.; Chen, Z.; He, H. A data-driven multi-scale extended Kalman filtering based parameter and state estimation approach of lithium-ion olymer battery in electric vehicles. *Appl. Energy* **2014**, *113*, 463–476. [CrossRef]
36. Xiong, R.; Sun, F.C.; He, H.W. Data-driven state-of-charge estimator for electric vehicles battery using robust extended Kalman filter. *Int. J. Automot. Technol.* **2014**, *15*, 89–96. [CrossRef]
37. Tian, Y.; Xia, B.; Sun, W.; Xu, Z.; Zheng, W. A modified model based state of charge estimation of power lithium-ion batteries using unscented Kalman filter. *J. Power Source* **2014**, *270*, 619–626. [CrossRef]
38. Alkaya, A. Unscented Kalman filter performance for closed-loop nonlinear state estimation: A simulation case study. *Electr. Eng.* **2014**, *96*, 299–308. [CrossRef]
39. Arasaratnam, I.; Haykin, S. Cubature Kalman filters. *IEEE Trans Autom. Control* **2009**, *54*, 1254–1269. [CrossRef]
40. Crisan, D.; Doucet, A. A survey of convergence results on particle filtering methods for practitioners. *IEEE Trans. Signal Process.* **2002**, *50*, 736–746. [CrossRef]
41. Chen, X.; Shen, W.; Dai, M.; Cao, Z.; Jin, J.; Kapoor, A. Robust adaptive sliding-mode observer using RBF neural network for Lithium-ion battery State of Charge estimation in electric vehicles. *IEEE Trans. Veh. Technol.* **2016**, *65*, 1936–1947. [CrossRef]
42. Lin, C.; Mu, H.; Xiong, R.; Shen, W. A novel multi-model probability battery state of charge estimation approach for electric vehicles using H-infinity algorithm. *Appl. Energy* **2016**, *166*, 76–83. [CrossRef]
43. Duong, V.-H.; Bastawrous, H.A.; Lim, K.; See, K.W.; Zhang, P.; Dou, S.X. Online state of charge and model parameters estimation of the LiFePO4 battery in electric vehicles using multiple adaptive forgetting factors recursive least-squares. *J. Power Source* **2015**, *296*, 215–224. [CrossRef]
44. He, H.; Xiong, R.; Guo, H. Online estimation of model parameters and state-of-charge of LiFePO4 batteries in electric vehicles. *Appl. Energy* **2012**, *89*, 413–420. [CrossRef]
45. Xiong, R.; He, H.; Sun, F.; Zhao, K. Evaluation on State of Charge Estimation of batteries with adaptive extended Kalman filter by experiment approach. *IEEE Trans. Veh. Technol.* **2013**, *62*, 108–117. [CrossRef]
46. Chaoui, H.; Golbon, N.; Hmouz, I.; Souissi, R.; Tahar, S. Lyapunov-based adaptive state of charge and state of health estimation for lithium-ion batteries. *IEEE Trans. Ind. Electron.* **2015**, *62*, 1610–1618. [CrossRef]
47. Xiong, R.; Sun, F.; Gong, X.; Gao, C. A data-driven based adaptive state of charge estimator of lithium-ion polymer battery used in electric vehicles. *Appl. Energy* **2014**, *113*, 1421–1433. [CrossRef]
48. Sun, F.; Xiong, R. A novel dual-scale cell state-of-charge estimation approach for series-connected battery pack used in electric vehicles. *J. Power Source* **2015**, *274*, 582–594. [CrossRef]
49. Wei, Z.; Meng, S.; Xiong, B.; Ji, D.; Tseng, K.J. Enhanced online model identification and state of charge estimation for lithium-ion battery with a FBCRLS based observer. *Appl. Energy* **2016**, *181*, 332–341. [CrossRef]

50. Dai, H.; Xu, T.; Zhu, L.; Wei, X.; Sun, Z. Adaptive model parameter identification for large capacity Li-ion batteries on separated time scales. *Appl. Energy* **2016**, *184*, 119–131. [CrossRef]
51. Zou, C.; Manzie, C.; Nešić, D. A framework for simplification of PDE-based lithium-ion battery models. *IEEE Trans. Control Syst. Technol.* **2016**, *5*, 1594–1609. [CrossRef]
52. Doyle, M.; Newman, J.; Gozdz, A.S.; Schmutz, C.N.; Tarascon, J. Comparison of modeling predictions with experimental data from plastic lithium ion cells. *J. Electrochem. Soc.* **1996**, *143*, 1890–1903. [CrossRef]
53. Kumaresan, K.; Sikha, G.; White, R.E. Thermal model for a Li-ion cell. *J. Electrochem. Soc.* **2008**, *155*, A164–A171. [CrossRef]
54. He, H.; Xiong, R.; Guo, H.; Li, S. Comparison study on the battery models used for the energy management of batteries in electric vehicles. *Energy Convers. Manag.* **2012**, *64*, 113–121. [CrossRef]
55. Ljung, L. Convergence Analysis of Parametric Identification Methods. *IEEE Trans Autom. Control* **1978**, *23*, 770–783. [CrossRef]
56. Li, D.; Ouyang, J.; Li, H.Q.; Wan, J.F. State of charge estimation for $LiMn_2O_4$ power battery based on strong tracking sigma point Kalman filter. *J. Power Source* **2015**, *279*, 439–449. [CrossRef]